A knowledge-based deformable surface model with application to segmentation of brain structures in MRI

Amir Ghanei [a,b], Hamid Soltanian-Zadeh [a,c,d], Kost Elisevich [a], Jeffrey A Fessler [b]

[a] Henry Ford Health System, Detroit, MI 48202
[b] Department of Electrical Engineering and Computer Science, University of Michigan, Ann Arbor, MI 48105
[c] Department of Electrical and Computer Engineering, University of Tehran, Tehran 14399, Iran
[d] Department of Radiology, Case Western Reserve University, Cleveland, OH 44106

ABSTRACT

We have developed a knowledge-based deformable surface for segmentation of medical images. This work has been done in the context of segmentation of hippocampus from brain MRI, due to its challenge and clinical importance. The model has a polyhedral discrete structure and is initialized automatically by analyzing brain MRI sliced by slice, and finding few landmark features at each slice using an expert system. The expert system decides on the presence of the hippocampus and its general location in each slice. The landmarks found are connected together by a triangulation method, to generate a closed initial surface. The surface deforms under defined internal and external force terms thereafter, to generate an accurate and reproducible boundary for the hippocampus. The anterior and posterior (AP) limits of the hippocampus is estimated by automatic analysis of the location of brain stem, and some of the features extracted in the initialization process. These data are combined together with *a priori* knowledge using Bayes method to estimate a probability density function (pdf) for the length of the structure in sagittal direction. The hippocampus AP limits are found by optimizing this pdf. The model is tested on real clinical data and the results show very good model performance[1].

Keywords: Deformable models, Hippocampus, MRI, Image segmentation.

1. INTRODUCTION

Deformable models are energy minimizing shapes that starting from and initial shape, deform until reach the minimum of energy. Deformable models proved to be more powerful than traditional edge detection and segmentation methods for application in medical images. The deformable models have numerous applications such as image segmentation, shape modeling, computer graphics and visualization, and pattern recognition. *Deformable surfaces* are three-dimensional (3D) models that are directly applicable to volumetric data. Compared to deformable contours, deformable surfaces are potentially more flexible, generate more consistent results, and are more powerful in extrapolating the parts of the boundaries with low or zero contrast. They are more user-interactive. They also can include measures such as elastic forces, to create a more consistent segmentation for consecutive slices.

We present a new *geometrically deformable surface model*. The model deforms by sum of its force terms until it reaches equilibrium. The geometry of the model surface is a polyhedral with triangular facets. The advantage of using this structure compared to an analytical surface is its flexibility in segmenting objects with complicated shapes. The model deforms by internal and external forces. Internal forces are calculated from local model curvature, using a least-squares error approximation to the Dupin indicatrix. Compared to other methods such as surface fitting, this method is more robust to noise, selection of coordinates axes, and parameters such as number of points used or local resolution of the surface. External forces are calculated by applying a step expansion and restoration filter (SEF) to the volumetric image data. A solution for one of the most common problems associated with deformable models, self-cutting, has been proposed in this work. We use a principal axis analysis and re-slicing of the deformable model followed by triangulation of the slices, to remedy self-cutting. We use vertex re-sampling, multi-resolution deformation, and refinement of the mesh grid to improve the quality of the model deformation, which leads to better results. We also present a method for generating an initial model from a stack of initial contours, drawn freely by the user on arbitrary slices of the volumetric data. Examples of the model application to different cases are presented, which show diversity and flexibility of the model.

[1] Correspondence: Amir Ghanei. Email: aghanei@umich.edu

Medical Imaging 2001: Image Processing, Milan Sonka, Kenneth M. Hanson, Editors,
Proceedings of SPIE Vol. 4322 (2001) © 2001 SPIE · 1605-7422/01/$15.00

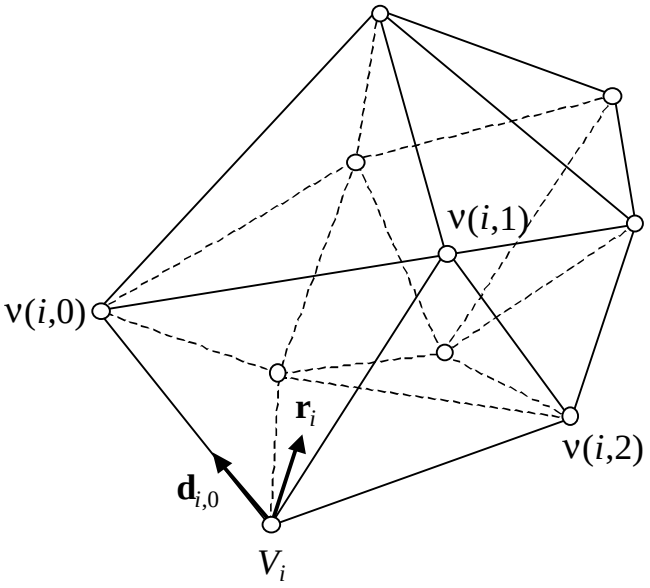

Fig. 1. A simple example of the model structure with 10 vertices. The relative indices of some of the neighbors of V_i have been shown. $\mathbf{r}_i$ is the unit radial (normal) vector at vertex i and $\mathbf{d}_{i,0}$ is the unit vector along the edge between V_i and $\nu(i,0)$.

1.1. Background

3D deformable models can be divided into two general categories of analytical and discrete models. In the analytical models, usually second or higher order algebraic surfaces are used. For example, Blokland, et al.[1] used ellipsoids for this purpose. Terzopoulos and Metaxas[2] used superquadrics, which is the extension of quadrics using an exponent that allows the shape to vary from an ellipsoid to a rectangular parallelepiped [3,4]. Nastar and Ayache used meshes [5]. Other forms of analytical surfaces exist such as cylinders, which are used by several authors like Terzopoulos, et al.[6] and Rao and Nevatia [7], and Fourier series which are used by Staib, et al.[8] to represent active surface components. This type of surface representation using its harmonics has been used by others as well [9,10]. Whitaker[11] introduced active blobs and used level sets of a scalar function to define the model surface. Zeng, et al.[12] employed level sets for creating coupled embedded deformable surfaces, which are used to extract the cortex from brain images. However, their method assume constant thickness for the cortex. Schlesinger, et al.[13] used a deformable geodesic model. They improved resolution of the basic geodesic by re-sampling. Although these surfaces use a relatively small number of parameters, they lack enough flexibility needed for segmenting complicated objects. Among the analytical functions for surface interpolation, B-splines recently have been favored by several authors. Huang, et al.[14] used a 4-D B-spline model for tracking the motion of the left ventricle of heart from tagged MRI. They have used simultaneous fitting of model knots to MRI frame data. Peterfreund [15] used snakes for position prediction of non-rigid objects by applying a velocity control to an elastodynamical contour model. Other types of parametric analytical deformable surfaces have been introduced in the literature as well [12,16,17]. In general, in the analytical models, algebraic formulation of the surface has the advantage of conciseness representation but it greatly limits expressiveness and flexibility of the model.

In the category of discrete 3D models, the model of Szeliski, et al.[18] used a discrete particle system. The energy minimizing surfaces of Cohen and coworkers[19] can be considered as a direct extension of the snake model to 3D. Terzopoulos and coworkers[20] used a crystal like cubic model, which is useful for facial modeling and animation. Their internal forces act like springs between vertices and try to pull the model points together. Kelemen, et al.[16] in their 3D model used the idea of active shape and point distribution models in the parameter space to calculate an average initial shape and corresponding eigenmodes. The deformation of the surface starts from the average shape and is restricted by these eigenmodes. Their model needs a common normalized coordinate system and the geometry of the shape is described in parameter space rather than explicitly, like our model. Ruffa, et al.[21] also used point distribution model for describing and estimating the shape from sparse data and volume measurement.

Among the 3D models, we should mention GDM (Geometrically Deformed Model) proposed by Miller, et al.[22], due to some of its similarities to this model. Their model is made by polygonal facets that form a closed surface, which evolves by local geometric constraints as well as image-defined costs. However, our model has fundamental differences from GDM. We use a LSE

approximation for estimation of the surface curvature and normal vector. In GDM, a measure calculated from the average distance between neighboring vertices is used. Their method is not effective for complicated shapes (*e.g.*, severely concaved shapes) and is weak for simple shapes. In our model, the deformation is based on force terms compared to cost functions of the reference [22]. Furthermore, the external energies in GDM usually have to be calculated by thresholding the image, due to the nature of the GDM evolution. This is different from our proposed model where user can use any filter. In addition, we proposed other mechanisms such as remedy of self-cutting, creation of initial model from arbitrarily drawn contours, and regridding the data to improve the performance, which has not been addressed in the GDM. The details are described throughout this paper.

2. PROPOSED METHODS

We use a point-wise triangular structure for the model surface. This representation of objects has been used in engineering fields such as aerospace and fluid mechanics for simulating the behavior of an object in the presence of external and internal forces. External forces used in these applications originate from the environment, *e.g.*, wind or gravity, and internal forces are caused by the structure of the object, *e.g.*, its tension, as described in the following sections.

2.1. Model structure

This section briefly describes the model geometry. The reader is referred to references [23,24,25] for more details. The model structure consists of a set of vertices and edges that form a closed surface defined by connected triangle facets (see Fig. 1). The position of vertex i, V_i, in the Cartesian space is represented by vector $\mathbf{p}_i$. Each vertex, like i, is directly connected to three or more vertices by edges. The kth neighboring vertex of V_i is shown by $v(i,k)$ ($0 \le k \le M_i - 1$, where M_i is the number of the neighboring vertices for V_i). Looking to V_i from outside of the volume perpendicular to the surface, the index k in $v(i,k)$ increases in clockwise direction. The edge between i and $v(i,k)$ is shown by $\mathbf{D}_{i,k}$:

$$\mathbf{D}_{i,k} = \mathbf{p}_{v(i,k)} - \mathbf{p}_i \ . \tag{1}$$

We use $\mathbf{d}_{i,k}$ to show the unit vector along $\mathbf{D}_{i,k}$ and $\mathbf{r}_i$ to show the unit vector normal to the model surface at V_i.

2.2. Model deformation

The model deforms under the influence of the internal and external forces. The external forces are extracted from the image features. In this work, external forces are defined to make the model converge to the object boundaries. The internal forces maintain the smoothness of the model by minimizing the surface curvature as described in the following section.

2.2.1. Internal forces

The internal forces are based on the local curvature of the surface. In this work, we use a least-squares error (LSE) estimation to the Dupin indicatrix for estimating the curvature and the surface normal[26]. The method is robust and relatively insensitive to the model resolution, number of points used for estimation, and choice of the coordinate system. After calculating the principal curvatures (maximum and minimum curvatures) for each vertex, κ_1 and κ_2, we consider the mean curvature, C_i, as the numerical value for the curvature at that vertex:

$$C_i = (\kappa_1 + \kappa_2)/2 \ . \tag{2}$$

Internal force at vertex i, $\mathbf{f}_{\text{in},i}$, is computed from the local curvature value, C_i and the curvatures of the neighboring vertices, $C_{v(i,k)}$, as:

$$\mathbf{f}_{\text{in},i} = \left\{ C_i - \frac{1}{M_i} \sum_{k=0}^{M_i - 1} C_{v(i,k)} \right\} \mathbf{r}_i \ . \tag{3}$$

The above definition sets the direction of $\mathbf{f}_{\text{in},i}$ along the radial vector. When $\mathbf{f}_{\text{in}}$ is the only acting force, the above internal forces push the initial shape towards a maximally smooth and closed surface, which has a general spherical shape. In practical situations, there are also external forces acting on the model, and the final shape depends on the relative weight of the two forces and will also be affected by the image data.

2.2.2. External forces

External forces push the model towards the minimum of an external energy, which is defined from the volume data using an appropriate operator. We use a Step Expansion Matching and Restoration (SEF) filter which has been introduced by Rao et al.[27]. It is an edge detector that uses expansion matching and restoration. It is optimal in the sense of a special figure of merit named

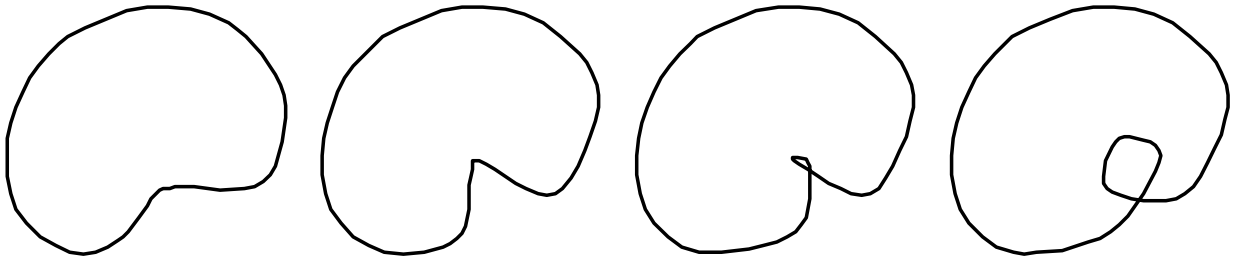

Fig. 2. 2D Illustration of development of self-cutting in the model. Self-cutting increases from left to right.

discriminative signal-to-noise-ratio[27]. Assuming the noise in the image can be modeled with white noise and the edge model is a step function, the impulse response of SEF filter in one dimension is

$$h(x) = \mathrm{sgn}(x)e^{-2|x|/\sigma} \tag{4}$$

where, σ^2 is the variance of the white noise and sgn(x) is the sign function.This above filter is applied to the volumetric image data in three perpendicular directions and the sum of the results is used as the image energy. The gradient of this image energy at each point define the local external force. The force applied to each vertex is the radial component of the local external force. Hence, we will have:

$$\mathbf{f}_{\mathrm{ex},i} = -(\nabla E_{im} \cdot \mathbf{r}_i)\,\mathbf{r}_i, \tag{5}$$

where E_{im} is the image energy defined by:

$$E_{im} = |h(x) * I| + |h(\mathrm{y}) * I| + |h(\mathrm{z}) * I| \tag{6}$$

where I represents the volumetric image data, and * is the convolution operator.

2.2.3. Deformation process

The deformation process is a result of internal and external forces acting on the model. The total force acting on each vertex is a weighted sum of $\mathbf{f}_{\mathrm{in}}$, $\mathbf{f}_{\mathrm{ex}}$ and a damping force, $\mathbf{f}_{\mathrm{damp}}$, which is set proportional to the vertex velocity, $\mathbf{v}_i$, and used to make the model more stable:

$$\mathbf{f}_{\mathrm{damp},i} = K_{\mathrm{damp}}\mathbf{v}_i, \tag{7}$$

where K_{damp} is a negative constant. The surface deformation is computed in discrete positions in time as follows:

$$\mathbf{p}_i(t+\Delta t) = \mathbf{p}_i(t) + \mathbf{v}_i(t)\Delta t \tag{8}$$

$$\mathbf{v}_i(t+\Delta t) = \mathbf{v}_i(t) + \mathbf{a}_i(t)\Delta t \tag{9}$$

$$\mathbf{a}_i(t+\Delta t) = \mathbf{f}_i(t+\Delta t)/\mathrm{m}_i \tag{10}$$

$$\mathbf{f}_i = w_{\mathrm{ex}}\mathbf{f}_{\mathrm{ex},i} + w_{\mathrm{in}}\mathbf{f}_{\mathrm{in},i} + w_{\mathrm{damp}}\mathbf{f}_{\mathrm{damp,i}} \tag{11}$$

where $\mathbf{a}_i$, $\mathbf{v}_i$ and m_i are vertex acceleration, velocity, and assigned mass, respectively. Δt is the time step and its value can influence the model convergence. We have used Δt = 1 Sec in each iteration. A larger value might jeopardize the convergence and too small values slow down the model.

The deformation process starts from an initial surface. Vertices will move according to the above equations until the model reaches equilibrium in which the total force acting on each vertex is zero. In practice, we use a threshold on the model velocity as a stopping criterion. In this method, it is assumed that convergence is achieved when the model movements are very small during several consecutive iterations.

For the model initialization, most of the authors have used a fixed shape. We have developed a specific method that gives the user flexibility in defining the initial shape. The model creates a closed surface from a stack of 2D contours that have been drawn on parallel cross sections. In our model, the initial shape will be produced in two steps. In the first step, appropriate vertices of the consecutive polygons are connected to each other in a specific order. In the second step, the first and the last polygons are broken into triangle facets, as explained in detail in reference[23].

2.3. Self-cutting

Self-cutting is a common problems in deformable models is that happens in certain configurations of image forces and contour shape (see Fig. 2). Once it starts, it usually increases during the evolution of the model. The issue is much more complicated for a 3D closed surface compared to a 2D contour. We did not find any feasible method to remedy the self-cutting directly in 3D, nor did we find any reference in the literature that addressed the problem. However, we developed and implemented the following method, which reduces the problem to self-cutting in 2D and solves it. Then, it reconstructs the 3D volume from the refined slices. The approach has the following steps.

1. Let $V_0,\ldots,V_{m-1}$ denote the subset of m vertices with highest curvatures. Let $\mathbf{p}_i = (x_i, y_i, z_i)$ be the coordinate vector for V_i. We compute the sample covariance matrix Ψ as:

$$\Psi = \frac{1}{m}\sum_{j=1}^{m}(\mathbf{p}_j - \overline{\mathbf{p}})(\mathbf{p}_j - \overline{\mathbf{p}})^T , \tag{12}$$

where $\overline{\mathbf{p}}$ is the estimated average vector:

$$\overline{\mathbf{p}} = \frac{1}{m}\sum_{i=1}^{m}\mathbf{p}_i . \tag{13}$$

The mean point $\overline{\mathbf{p}}$ and the (orthogonal) eigenvectors of Ψ define a new m dimensional coordinate system with $\overline{\mathbf{p}}$ as the origin. The main axis of the model is along the eignevector cooresponding to the largest eignevalue, call it $\mathbf{b}_0$.

2. We define a set of parallel planes $S_0, S_1, \ldots, S_{K-1}$ where plane S_i is defined by:

$$\mathbf{b}_0 \cdot (\mathbf{x} - \mathbf{x}_i) = 0 , \tag{14}$$

where $\mathbf{x}$ is any point on S_i and $\mathbf{x}_i$ is:

$$\mathbf{x}_i = \overline{\mathbf{p}} - (i - \frac{K}{2}) \cdot l_r \cdot \hat{\mathbf{b}}_0, \qquad 0 \le i \le K-1, \tag{15}$$

where l_r is the model resolution and $\hat{\mathbf{b}}_0$ is the unit vector along the principal axis. K is chosen such that the range of $\mathbf{x}_i$s cover the entire 3D volume. The intersection of S_i with the model is a closed contour which we show by C_i. To obtain C_i, first we find the intersection of S_i with all the peripheral sides of the polyhedral, which gives a set of segments. Then, an edge tracking method is applied to the obtained points which returns the same set of points but in clock-wise rotation order.

3. All the C_is are resampled to keep the resolution equal to the model resolution l_r. In the next step, each contour is checked for self-cutting. If an intersection shows existence of a loop, we compare the circumference of the loops, and the smaller loop is deleted by directly connecting the two segments that are intersecting. We tested this method at it proved to be very effective. Now, a new 3D model is constructed from the set of closed contours $C_0, C_1, \ldots, C_{K-1}$ using the method described in the following section, in which self-cutting is corrected from the surface.

After removal of self-cutting, deformation continues. This fixes any artifacts in the form of alteration of the shape that can result from reslicing and reconstruction procedure described above. This procedure is fast and it is usually necessary to be applied only once or twice to the model during the deformation.

2.4. Segmentation of hippocampus from MRI

The hippocampus is an important component of the human brain's limbic system (see Fig. 3). It is strongly believed that this structure has a key role in learning process and memory. The variation in volume and architecture of this structure has been observed with some brain diseases such as schizophrenia, epilepsy, and Alzheimer [28,29]. At the time of this writing, one in every 200 people within the United States (US) suffers from a neurological disease referred to as "epilepsy". Two-thirds of all epileptic patients have a specific focal area of seizure onset within the brain. More than 20% of the epileptic patients undergo surgery when treatment with medication is ineffective, *i.e.*, nearly 250,000 patients are potential candidates for epileptic surgery in the US. The conventional method of evaluating an epileptic patient for surgical candidacy is lengthy, painful, and expensive. It requires EEG exams to detect "irritative zones".

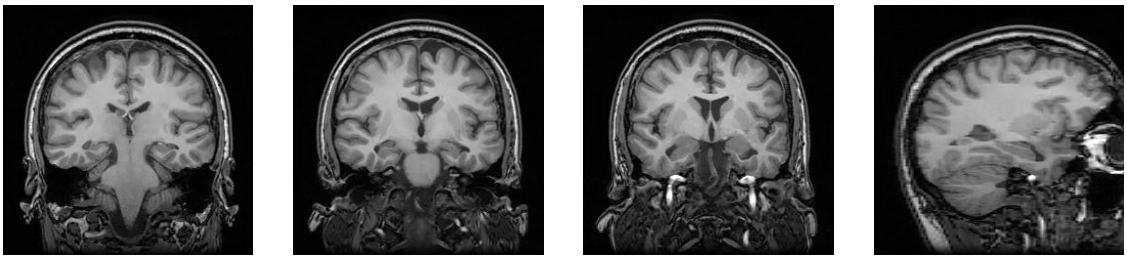

(a) (b) (c) (d)

Fig. 3. Figures of hippocampus in T1-weighted images of brain MRI. (a)-(c) coronal images from posterior towards the anterior; (d) sagittal view.

The method in this paper has been developed in hope to establish specific and sensitive means of identifying foci of epileptogenicity from MRI. This will allow for a more contracted electrographic investigation by focusing attention into the abnormal site. The results will be reducing the diagnosis cost for a majority of patients.

Our developments are based on recent research results indicating that determination of structural and volumetric asymmetries in the human brain from MRI provides critical data for the diagnosis of focal abnormality. This has been the case with complex partial seizures attributable to hippocampal sclerosis and has been further applied to other brain regions for the same purpose. In many cases, volumetric analysis of the hippocampus from MRI is recommended for human[30] and animal studies[31]. Conventional methods for this determination (manual segmentation of structures from MRI) are labor-intensive, costly, require an expert operator, and are not reproducible. These problems are most appreciated when detecting small differences that are undetectable by visual inspection of the images. For example, a study in the Henry Ford Health System (Detroit, MI) showed a huge variability for the hippocampi volumes calculated from MRI studies of 11 patients, using manual segmentation of the hippocampi by two physicians. The percent difference between the hippocampi volumes determined by the two physicians ranged from 3% to 133% and averaged at 57%[32]. In addition, these problems are limiting factors in multi-institutional studies and in comparing quantitative results reported by different research groups. Because of these problems, extraction of quantitative information from MRI is currently done by a limited number of medical institutions. Automated procedures are expected to solve the above problems, thereby making it possible for most medical institutions to benefit from quantitative information extracted from MRI for patient care. However, segmentation of the hippocampus with conventional methods, *e.g.*, filtering, thresholding, or region growing does not give satisfactory results, because this structure has relatively low contrast, multiple edges, and also discontinuous edges in MRI. Deformable models have been proposed for the segmentation of the hippocampus[16,23,24], and other brain structures from MRI[33] and are desirable due to their unique properties such as integrity and treating the object as a whole.

We present a two-stage method for segmentation of the hippocampus. First a knowledge-based method for the localization of the hippocampus, which is developed by Siadat and Soltanian-Zadeh[34,35] will be used. In the second part, we incorporate a knowledge-base into the deformable model for accurate segmentation of the hippocampus. The proposed method of Siadat and Soltanian-Zadeh finds the majority of the slices which contain hippocampus and locates a few points around the structure automatically on them. This is done using the image information and a set of logical rules, defined based on the anatomy of the human brain. They developed an expert system for using the rules in analyzing the information extracted from MRI. Some of the features extracted by expert system in the first stage and localization result are used by the extended 3D deformable model to accurately segment the hippocampus.

2.4.1. A rule-based system for localization of hippocampus

We have incorporated a rule-based expert system proposed by Siadat and Soltanian-Zadeh[34,35] for localization of hippocampus. This system examined the 2D coronal slices of the brain dataset one by one and after thresholding each slice to create CSF, gray matter (GM) and white-matter (WM) maps, it tries to identify important anatomical landmarks such as ventricles and Sylvian fissure. Based on identification of these landmarks and the shape of the corresponding structures and their relative position and size, this system decides if that slice contains hippocampus and tries to find three points on the boundary of the hippocampus. These procedures are based on pixel-by-pixel search of the binary images and a set of if-then rules that are based on the *a priori* knowledge of the brain anatomy applied within an expert system scheme. The detail of the algorithm used can be read in[34,35]. In the rest of this paper, we discuss incorporation of the localization results in the 3D deformable model and other aspects of the hippocampus segmentation.

2.4.2. Using the results of the localization

The localization stage finds 3 to 4 points around left and right hippocampus in majority of the slices that contain this structure. This data is used for initialization and deformation of the 3D model. In the initialization phase, we use a triangulation method to

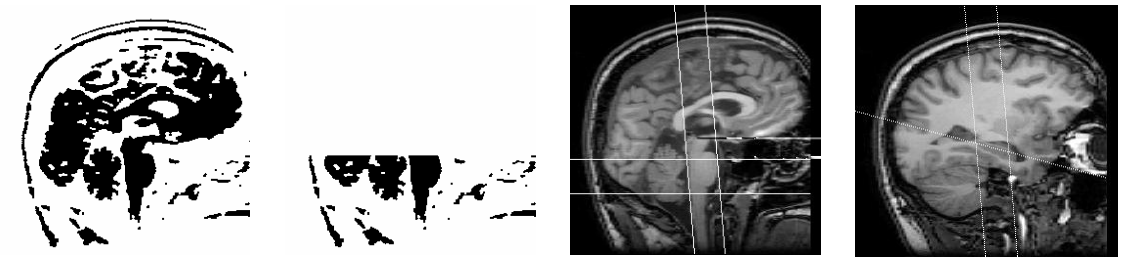

(a) (b) (c) (d)

Fig. 4. An example of automatic extraction of brainstem and its application for estimation of hippocampus anterior and posterior limits. (a) Binary image obtained by automatic detection of brain midplane and thresholding it. (b) Image in (a) masked in area above search point. (c) The resulting tangential lines overlaid on the midplane image. The horizontal lines show the vertical range of the part of the brainstem analyzed. (d) The tangential lines of the brainstem and the model axis overlaid on the sagittal slice through the hippocampus.

connect the appropriate vertices in consecutive slices together, and build the initial model structure. This initial shape will be used to start the deformation process and find the accurate boundaries.

2.4.3. Model length

As we explained, hippocampus is elongated in the sagittal direction. One of the points of debate has been a reproducible method for finding the length of this structure (its anterior and posterior limits). Jack, et al[29] defined the posterior boundary of the hippocampus as the oblique coronal plane intersecting the posterior commissure on the midline sagittal slice, and the anterior limit as the intersecting oblique plane parallel to the above oblique plane, passing through tangent to the anterior border of the splenium of the corpus callosum.

Our approach is inspired from the above definition, however it uses the brainstem as a major landmark. Instead of passing the tangential line through posterior commissure, we use the line tangential to the posterior and anterior limits of the brainstem in the midline sagittal plane. We use the landmarks in conjunction with a Bayesian probability model, which is used to complete the above approach. This method optimizes a MAP estimator for the hippocampus AP limits. The details are described in the following section.

2.4.3.1 Initial estimation by automatic landmark analysis

We use the following method to detect the starting and ending coronal slice for the hippocampus. In the first step, we use an automatic method to extract the brainstem boundaries as follows (see Fig. 4):

1. Using the method described in the previous section, the thresholds for CSF, GM, and WM is found.
2. The center of mass of the 3D model is found and is called C. The coronal slice passing through C is denoted I_C, which is thresholded to eliminate the background. The resulting binary image is used to find the center of I_C, call it O.
3. The sagittal image I_O which passes through O is used as the brain inter-hemisphere slice. We use WM gray level range to threshold I_O. We apply erosion and dilation to eliminate isolated points. I_O is masked above point O. (see Fig. 4(b))
4. We search the binary image I_O from point O within 250° to 290° range (270° is 6:00 O'clock). The search procedure finds one point of the brainstem (BS) structure. We use FCC to extract the whole BS from this initial seed.
5. We make a tangential to the posterior edge of the BS, call it T_p, and a line parallel to this tangential line from the most anterior point of the BS, call it T_a.
6. Using the least-squares error fitting, a line is passed through the model in oblique direction. This line approximately represents the model axis. The intersection points of the projection of this line on I_O with T_a and T_p are used to estimate the anterior and posterior limits of the hippocampus. Z_{ba} and Z_{bp}, represent the Z coordinates of these two points respectively (assuming the Z axis is along sagittal direction).

2.4.3.2 Bayesian approach for estimation of hippocampus limits

We use *a priori* knowledge and the Bayes rule to estimate AP limits of the hippocampus. Let Z denote the slice location (in sagittal direction). To find the AP limits of hippocampus, we use the following procedure. For each Z, the probability of Z being the most anterior or posterior Z of the hippocampus structure, shown by Z_s, is calculated by the following formula:

Table 1. Comparison between the model results and manual segmentation for 29 patients. All the units are pixels. OR, AND, and XOR show the result of application of corresponding pixel-wise operator to the areas on and inside manual and automatic contours. The Similarity and Difference are calculated using the Kappa statistics.

Patient	Distance	OR	AND	XOR	Similarity	Difference
1	1.22	232	140	92	60	39
2	1.24	244	154	89	63	36
3	1.02	172	113	59	65	34
4	1.19	275	182	93	66	33
5	1.60	230	138	91	60	39
6	0.98	260	172	88	66	33
7	1.23	221	158	63	71	28
8	1.65	319	195	123	61	38
9	1.20	301	205	95	68	31
10	1.85	304	167	137	54	45
Average	1.32				63.4	26.6
Stdv	0.28				5.21	5.21

$$P_s(Z) = P(Z = Z_s \mid \mathbf{D}_Z) = \frac{P(\mathbf{D}_Z \mid Z = Z_s)P(Z_s)}{P(\mathbf{D}_Z)}. \tag{16}$$

We calculate $P_s(Z)$ for all the slices. The posterior and anterior limits, Z_{hp} and Z_{ha}, are found as follows:

$$Z_{hp} = \max_Z P_s(Z), \text{ for } 0 \le Z \le Z_{bp}. \tag{17}$$

Similarly

$$Z_{ha} = \max_Z P_s(Z), \text{ for } Z_{ap} \le Z \le Z_{max}. \tag{18}$$

$\mathbf{D}_Z$ is defined as:

$$\mathbf{D}_Z = \lfloor \mathrm{CNF}_1(Z) \quad \mathrm{CNF}_2(Z) \quad \cdots \quad \mathrm{CNF}_K(Z) \quad b_a(Z) \quad b_p(Z) \rfloor, \tag{19}$$

which is a 1×(K+2) row vector containing the different CNF factors at the slice located at Z, which is calculated by the expert system as explained in Appendix A, and $b_a(Z)$ and $b_p(Z)$ are defined using Z_{ba} and Z_{bp} (defined in the previous section), respectively as:

$$b_a(Z) = \frac{Z_{ba} - Z}{L_n}, \tag{20}$$

and L_n is the normalization factor used to compensate for the effect of the brain size, and defined as the length of the brain from most anterior to the most posterior point. $b_p(Z)$ is calculated similarly.

Table 2. Comparison and ranking the segmentation quality of the model, the collaborating neurosurgeon, a neuroradiologist, and a radiologist, as judged by the neurosurgeon (blinded). 1 is assigned the best contour and 4 to the worst.

Patient	Average rank			
	Model	Neurosurgeon	Neuroradiologist	Radiologist
1	2.22	1.67	3.56	2.56
2	1.46	2	3.77	2.77
3	1.67	1.93	3.53	2.93
4	2.14	1.86	3	3
5	1.73	1.73	3.44	2.87
6	1.5	3	1.5	4
Average	1.79	2.03	3.13	3.02

3. RESULTS

We have implemented and tested the above methods. Some of the examples of model results and statistical evaluation of its performance is presented below.

Table 1 shows the comparison between the model results and manual segmentation for 10 patients. Similarity is measured as the number of pixels common in both of the contours (pixel-wise AND), divided by the total number of pixels (pixel-wise OR). This similarity measure approximates the Kappa statistics. It can be seen that the average similarity is about 63%, which is a very good match. Note that hippocampus has a very small area, making the similarity measure very sensitive. The average distance of the model contours from the manual contours is 1.3 pixels (about 1 mm), which is very good.

The numbers in Table 1 should be judged by comparing to the statistics of agreement between different manual contours generated by different experts, which have been about 54% for the same patients. As it can be seen, the agreement between the model and the neurosurgeon is more than the agreement between any two different experts.

We presented contours from the slices of the model results, and the contours drawn by the collaborating neurosurgeon, a neuroradiologist, and a radiologist to the neurosurgeon blinded to the source of the contours, slice by slice. The neurosurgeon is an expert in treating epileptic patients and hippocampus surgery. In each slice, he has ranked the contours from best (1) to worst (4), in terms of representation of the hippocampus. In Table 2 we presented cumulative results for each patient. The numbers for each method has been averaged for each patient. The overall statistics for all of the patients shows the average ranking of 1.8 for the model, 2 for the neurosurgeon, 3.1 for the neuroradiologist, and 3 for the radiologist. This means that the model segmentation received the best rank compared to other segmentations.

ACKNOWLEDGEMENT

The authors would like to thank Dr. Suresh Patel and Dr. Cylen Javidan-Nejad from Henry Ford Health System for their help in evaluation of the model. This work was supported in part by the NSF grant BES-9911084.

REFERENCES

1. Blokland, A Vossepoel, A Bakker, et al. Delineating elliptical objects with an application to cardiac scintigrams. *IEEE Trans. Med. Imag.*, 6(1): 57-66, 1987.
2. D Terzopolous, D Metaxas. Dynamic 3D models with local and global deformations: deformable superquadratics, *IEEE Trans. Patt. Anal. Mach. Intell*, PAMI 13(7): 703-714, 1991.
3. E Bardient, LD Cohen, N Ayache. Fitting of iso-surfaces using superquadrics and free-form deformations. *Proc. IEEE Workshop Biomed. Imag. Anal.*, 184-193, 1994.
4. F Solina, R Bajcsy. Recovery of parametric models from range images: the case for superquadrics with global deformaion, *IEEE Trans. Patt. Anal. Mach. Intell.*, PAMI 12(2): 131-147, 1990.
5. C Nastar, N Ayache. Non-rigids motion analysis in medical images: a physically based approach. *Barret and Gmitro*, 23: 17-32, 1990.
6. D Terzopolous, A Witkin. Constraints on deformable models: recovering 3D shape and nonrigid motion, *Art. Intell.*, 36(1): 91-123, 1998.
7. K Rao, N Nevatia. Computing volume descriptions from sparse 3D data. *Int'l J. Comput. Vision*, 2(1): 33-50, 1988.

8. LH Staib, JS Duncan. Model-based deformable surface finding for medical images. *IEEE Trans. Med. Imag.,* 15(5): 720-731, 1996.
9. DH Ballard, CM Brown. Computer Vision. Englewood Ciffs, NJ: Prentice-Hall, 1982.
10. RB Schudy. Harmonic surfaces and parametric image operators: their use in locating the moving endocardial surface from three dimensional cardiac ultrasound data. *Computer Science Tech. Rep.* 112, Univ. of Rochester, Rochester, NY, 1981.
11. RT Whitaker. Volumetric deformable models: active blobs, SPIE, 2359: 122-134, 1992.
12. X Zeng, LH Staib, RT Schultz, and JS Duncan, Segmentation and measurement of the cortex from 3-D MR images using coupled-surfaces propogation, *IEEE Trans. Med. Imag.*, 18(10): 927-937, 1999.
13. DJ Schlesinger, JW Snell, LE Mansfield, et al. Segmentation of volumetric medical imagery using multiple geodesic-based active surfaces. *SPIE*, 2710: 243-253, 1996.
14. J Huang, D Abendschein, VG Davila-Roman, AA Amini, Spatio-temporal tracking of myocardial deformations with a 4-D B-spline model from tagged MRI, *IEEE Trans. Med. Imag.*, 18(10): 957-972, 1999.
15. N Peterfreund. Velocity snake: Deformable contour for tracking in spatio-velocity space. *Computer Vision and Image Understanding*, 73(3): 346-356, 1999.
16. A Kelemen, G Szekely, G Gerib. Elastic model-based segmentation of 3-D neuroradiological data set. *IEEE Trans. Med. Imag.*, 18(10): 828-839, 1999.
17. T McInerney, D Terzopoulos, Topology adaptive deformable surfaces for medical image volume segmentation. *IEEE Trans. Med. Imag.*, 18(10): 840-850, 1999.
18. R Szeliski, D Tonnesen, D Terzopoulos. Modeling surfaces of arbitrary topology with dynamic particles, *Proc. 4th Int'l Conf. Comput Vision* (ICCV'93): 82-87, Berlin, Germany, 1993.
19. I Cohen, D Cohen, N Ayache. Introducing new deformable surfaces to segment 3D image. IEEE Conf. *Comput. Vision. Patt. Recog.*, 738-740, 1991.
20. D Terzopoulos, K Waters. Physically-based facial modeling, analysis, and animation, *J. Visual Comput. Animation*, 1: 73-80, 1990.
21. CF Ruffa, SW Hughes, DJ Hawkes, Volume estimation from sparse planar images using deformable models. *Image and Vision Computing*, 17(8): 559-565, 1999.
22. V Miller, DE Breen, WE Lorensen, et al. Geometrically deformed models: a method to extract closed geometric models from volume data. *Comput Graphics*, 25: 217-26, 1991.
23. A Ghanei, H Soltanian-Zadeh, JP Windham. Segmentation of the hippocampus from brain MRI using deformable contours. *Computerized Medical Imaging and Graphics*, 22(3): 203-216, 1998.
24. A Ghanei, H Soltanian-Zadeh, JP Windham. A 3D deformable surface model for segmentation of objects from volumetric data in medical images. *Computers in Biology and Medicine*, 28(3): 239-253, 1998.
25. A Ghanei, H Soltanian-Zadeh, M Jacobs, S Patel. Boundary-based warping of brain MR images. *J. Magn. Reson. Imag.*, 12(3): 417-429, 2000.
26. PH Todd, RJY McLeod. Numerical estimation of the curvature of the surfaces. *Comput. Aided Design*, 18(1): 33-37, 1985.
27. KR Rao, J Ben-Arie. Optimal edge detection using expansion matching and restoration. *IEEE Trans. Patt. Anal. Mach. Intell.*, PAMI 16: 1169-82, 1994.
28. F Cendes, F Andermann, P Gloor, et al. MRI volumetric measurement of amygdala and hippocampus in temporal lobe epilepsy. *Neurology*, 43(4): 719-25, 1993.
29. CR Jack, RC Petersen, PC O'Brien, et al. MR-based hippocampal volumetry in the diagnosis of Alzheimer's disease. *Neurology*, 42(1): 183-188, 1992.
30. U Bick, A Sprinz, J Weglage, et al. Computer-assisted MRI-volumetry of the amygdala and hippocampus in healthy young adults with a history of febrile convulsions in childhood. *Proc. of Computer Assisted Radiology and Surgery* (CAR'97), 101-104, Netherlands, 1998.
31. F Ohl, T Michaelis, H Fujimori, et al. Volumetric MRI measurements of the tree shrew hippocampus. *J. Neuroscience Methods*, 88(2): 189-93, 1999.
32. JJ Hasenau, Masters thesis, Wayne State University, Detroit, MI, 1997.
33. BM Dawant, SL Hartmann, JP Thirion, et al. Automatic 3-D segmentation of internal structures of thehead in MR images using a combination of similarity and free-form transformations: I. Methodology and validation on normal subjects. *IEEE Trans. Med. Imag.*, 18(10): 909-16, 1999.
34. MR Siadat, H Soltanian-Zadeh. An intelligent approach for locating hippocampus in human brain MRI. *Proc. 16th International Conference on Applied Informatics* (AI'98), IASTED, Germany, Feb. 1998.
35. H Soltanian-Zadeh, MR Siadat. Knowledge-based localization of hippocampus in human brain MRI. *SPIE*, 3661: 1646-55, 1999.